Kinetic Pattern Formation at Solid Surfaces*

Joachim Krug

Institut für Theoretische Physik, Universität zu Köln, 50937 Köln, Germany
krug@thp.uni-koeln.de

Die Form ist überall dieselbe, und muss es auch,
denn ein *Geist ist, der sie denkt.*[2]
Johann Wilhelm Ritter

1 Introduction

The emergence of regular spatial patterns from inanimate natural processes has been a source of fascination and wonder since the beginnings of scientific exploration. A quantitative understanding of the mechanisms underlying pattern formation is a rather recent achievement, which has been possible through a strong concerted research effort in nonlinear physics and mathematics during the past two or three decades. This, by now classic, body of work [1] has been mostly concerned with pattern formation phenomena in macroscopic systems, such as hydrodynamic instabilities and chemical oscillations. More recently, patterns in granular materials such as sand ripples have also been addressed from related points of view [2, 3].

The focus of the present contribution is on submicron-scale patterns like mounds, ripples and step bunches, which form on solid surfaces under nonequilibrium conditions. This subject differs from macroscopic pattern formation in that (i) the visualization of the patterns of interest requires advanced microscopy techniques, notably scanning probe microscopes, and (ii) the formation of the patterns often relies on specific atomic processes, which must be analyzed in detail to reach quantitative agreement between theory and experiment [4]. Nevertheless a phenomenological continuum approach to pattern formation at solid surfaces has been developed, to some extent in analogy to the established macroscopic theories of pattern formation. Such an approach has proven to be useful, because it allows for a compact, unified description of a variety of mechanisms, as well as for the efficient analytical or numerical modeling of global aspects of the surface morphology.

* To appear in *Collective Dynamics of Nonlinear and Disordered Systems*, ed. by G. Radons, P. Häussler and W. Just (Springer, Berlin 2004).

[2] *The shape is the same everywhere, as it has to be, because it is conceived by* one *mind.*

The purpose of this article is to provide an elementary introduction to the continuum approach. The article is based on lectures on pattern formation during epitaxial growth and erosion, which were delivered jointly with Thomas Michely. In addition to the topics covered in these lectures, phenomena related to surface electromigration and steering (the deflection of the trajectories of depositing atoms due to the attraction by the growing film surface) will be included here. The lectures also addressed atomistic aspects of growth and erosion, and the detailed relationship between the atomistic and continuum viewpoints. As extensive recent reviews on these issues are available elsewhere [4, 5, 6, 7], they will be treated only briefly here. We further emphasize that we are concerned only with *kinetically* (rather than energetically) driven morphological instabilities. This excludes the formation of hill-and-valley structures at thermodynamically unstable surfaces, as well as the broad class of patterns which form in heteroepitaxial growth due to the strain caused by the lattice mismatch between the substrate and the growing film [6, 7, 8].

The basic instability mechanisms are described in the next section. Section 3 discusses the emergence of the characteristic length scale of the patterns in the early time regime, while in Sect. 4 the nonlinear, late time evolution is discussed. Experimental examples are presented as appropriate to illustrate the theoretical concepts.

2 Instability Mechanisms

The basis of the continuum theory is the description of the surface morphology in terms of the height function h, which gives the surface position $z = h(\boldsymbol{r}, t)$ above a point $\boldsymbol{r} = (x, y)$ in the substrate plane at time t. The height function satisfies an evolution equation of the general form

$$\frac{\partial h}{\partial t} = \mathcal{F}(\nabla h, \nabla^2 h, ...) \,, \tag{1}$$

where the function $\mathcal{F}$ must be chosen appropriately to encode the processes that contribute to the morphological evolution. It depends on the derivatives of h but is independent of the height itself, because the evolution is invariant under constant shifts of the reference plane, $h \to h+C$. Moreover, the function $\mathcal{F}$ is constructed such that the evolution equation always admits solutions corresponding to a flat, featureless surface, either parallel to the reference plane, or, more generally, inclined relative to the reference plane with a tilt vector $\boldsymbol{m}$. In growth and erosion processes the mean height of the flat surface grows or recedes with some velocity v. The general flat solution of (1) is therefore of the form

$$h_0(\boldsymbol{r}, t) = \boldsymbol{m} \cdot \boldsymbol{r} + vt \,. \tag{2}$$

The emergence of a pattern on the surface is signalled by the instability of the flat solution (2). In the following subsections, the leading order contributions

to $\mathcal{F}$ corresponding to various nonequilibrium processes will be derived, and the conditions for morphological instability will be explored.

2.1 Epitaxial Growth

In epitaxial growth from an atomic or molecular beam, atoms arrive at the surface at a rate set by the deposition flux F. They diffuse as *adatoms* over the atomically flat terraces and are incorporated into the crystal at steps of monoatomic height. As each step separates an upper and a lower atomic terrace, the incorporation of atoms can occur either from above or from below. Using field ion microscopy, Ehrlich and Hudda discovered in 1966 that diffusing adatoms tend to be reflected when they approach a descending step from above [9]. This implies that incorporation into steps is typically more facile from the lower terrace, and that *interlayer transport*, which involves step crossing, is reduced compared to the transport within one atomic layer. The corresponding potential energy landscape experienced by the adatom is illustrated in Fig. 1.

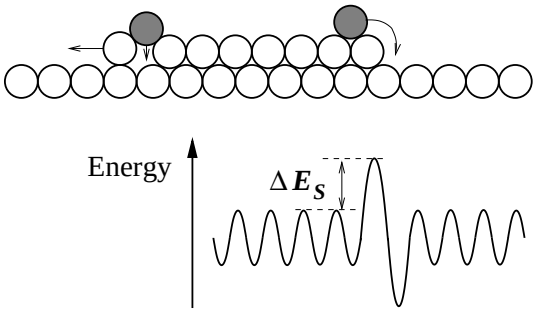

Fig. 1. The upper part of the figure shows the descent of adatoms (*shaded*) from an island. The adatom on the right descends through hopping, while the adatom on the left descends by exchanging its position with a step atom. The lower part of the figure illustrates the potential energy landscape experienced by the descending adatom on the right; the potential minima are aligned with the corresponding adsorption sites on the surface. The descent into the favorable position at the step edge is hindered by an additional step edge energy barrier ΔE_S. In the case of hopping, the existence of an additional barrier can be attributed to the poor coordination of the adatom in the transition state. The exchange process on the left allows the descending adatom to maintain the coordination to its neighbors, but it requires to move two atoms rather than just one

The Villain Instability

Jacques Villain first developed a continuum picture which shows that the step edge barrier illustrated in Fig. 1 generically implies a morphological

instability of the growing surface [10]. The essence of his argument is depicted in Fig. 2. It shows a small bump on the surface which may have been formed through a random fluctuation. The terraces on the slopes of the bump are bounded by one descending and one ascending step, and are called *vicinal* terraces. Because of the step edge barrier, the atoms deposited onto these terraces attach preferentially to the ascending step. The figure shows how this implies a net displacement of each adatom, between its point of impact and its point of incorporation, which is, on average, in the *uphill* direction. Within the continuum description, this implies a net mass current $\boldsymbol{j}(\nabla h)$, which is a function of the local slope ∇h. Assuming isotropy within the reference plane, the current can be written in the form

$$\boldsymbol{j}(\nabla h) = f(|\nabla h|^2)\, \nabla h \; . \tag{3}$$

The current is uphill when $f > 0$.

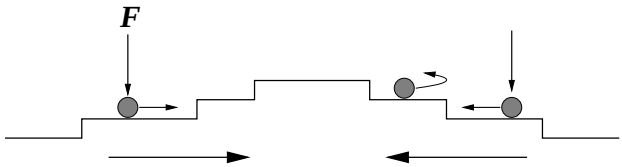

Fig. 2. Mechanism underlying the Villain instability (see text)

It is intuitively plausible that an uphill current will cause the bump to grow, and thus destabilize the surface. To analyze the instability in mathematical terms, we write down a surface evolution equation of the form (1). The mean film height grows at rate F, and the current $\boldsymbol{j}$ redistributes the deposited mass without changing the volume of the growing film. This implies a continuum equation of conservation type,

$$\frac{\partial h}{\partial t} = -\nabla \cdot \boldsymbol{j} + F \; , \tag{4}$$

which is obviously satisfied by the flat solution (2) with $v = F$.

For the time being, we specialize to a horizontal surface [$\boldsymbol{m} = 0$ in (2)]. To probe the stability of the flat state, we insert the ansatz $h(\boldsymbol{r}, t) = Ft + \varepsilon(\boldsymbol{r}, t)$ into (4) and expand to linear order in ε. This yields

$$\frac{\partial \varepsilon}{\partial t} = -f(0)\nabla^2 \varepsilon \; , \tag{5}$$

a diffusion equation with diffusion coefficient $-f(0)$. A linear partial differential equation like (5) is most conveniently solved by Fourier transformation. We make the ansatz for a perturbation of wavevector $\boldsymbol{q}$,

$$\varepsilon(\boldsymbol{r}, t) = \varepsilon_0 \mathrm{e}^{\mathrm{i}\boldsymbol{q}\cdot\boldsymbol{r} + \omega(\boldsymbol{q})t} \; , \tag{6}$$

and insert it into (5). We find that the growth rate of the perturbation is $\omega(\boldsymbol{q}) = f(0)|\boldsymbol{q}|^2$. Thus the flat state is unstable (the perturbation grows) when $f(0) > 0$. Through the uphill current that it causes, the step edge barrier implies a *mound instability* of the growing surface. An experimental example of the mound morphology caused by this effect is shown in Fig. 3 (see [11] for details).

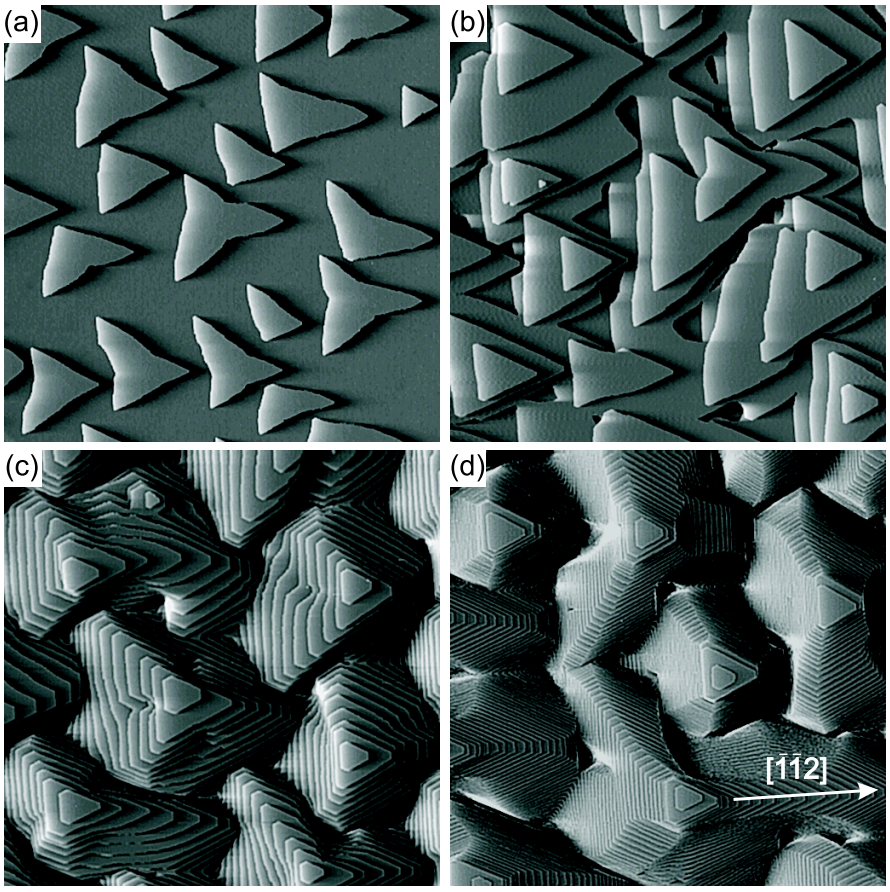

Fig. 3. Scanning tunneling microscope images of a Pt(111) surface after deposition of (**a**) 0.35 monolayers (ML), (**b**) 3 ML, (**c**) 12 ML and (**d**) 90 ML of platinum [11]. The growth temperature was 440 K and the deposition flux $F = 7 \times 10^{-3}$ ML/s. The triangular shape of the islands and mounds reflects the threefold symmetry of the fcc(111) surface. The image size is 3450 Å$\times$ 3450 Å. Note that the different images do not show the same sample location. Courtesy of Thomas Michely

Vicinal Surfaces

It is straightforward to generalize the above stability analysis to surfaces of nonzero tilt [$\boldsymbol{m} \neq 0$ in (2)]. Without loss of generality, the tilt vector can be chosen along the x-axis, i.e. $\boldsymbol{m} = (m, 0)$ (see Fig. 4). We then find the following anisotropic generalization of (5):

$$\frac{\partial \varepsilon}{\partial t} = \nu_{\parallel} \frac{\partial^2 \varepsilon}{\partial x^2} + \nu_{\perp} \frac{\partial^2 \varepsilon}{\partial y^2} \, , \tag{7}$$

where the coefficients are given by [12, 13]

$$\begin{aligned} \nu_{\parallel} &= -[f(m^2) + 2f'(m^2)m^2] = -\mathrm{d}j/\mathrm{d}m \\ \nu_{\perp} &= -f(m^2) = -j(m)/m \, , \end{aligned} \tag{8}$$

and $j(m) = mf(m^2)$ is the one-dimensional version of the current (3). The growth rate of a general perturbation (6) is now found to be $\omega(\boldsymbol{q}) = -\nu_{\parallel} q_x^2 - \nu_{\perp} q_y^2$. Thus the coefficients $\nu_{\parallel}$ and $\nu_{\perp}$ govern the stability of the surface against perturbations parallel to the tilt (with wavenumber q_x) and perpendicular to the tilt (with wavenumber q_y), respectively.

A perturbation parallel to the tilt implies that the initially uniform spacing between the surface steps becomes modulated. If such a perturbation is amplified (i.e., if $\nu_{\parallel} < 0$), the surface undergoes a *step bunching* instability, in which it breaks up into regions of high step density (the step bunches) separated by wide flat terraces. A perturbation perpendicular to the step implies that the individual steps become wavy, hence $\nu_{\perp} < 0$ implies that the surface undergoes a *step meandering* instability. Because steps cannot cross, the meander can be accomodated only if the steps are deformed in phase with each other.

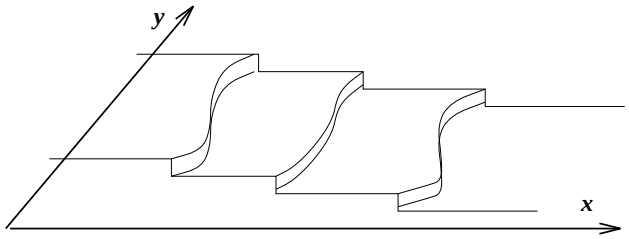

Fig. 4. Sketch of a vicinal surface

To evaluate the coefficients $\nu_{\parallel}$ and $\nu_{\perp}$, we need to specify the function $f(\nabla h)$ in (3). We consider a *vicinal surface* of the staircase shape shown in Fig. 4, which is composed entirely of vicinal terraces; it consists of steps of a single sign, which run on average along the y–axis and form no closed loops (i.e., adatom or vacancy islands). Such a surface shape is maintained

during growth, if each adatom deposited onto a terrace is able to reach one of the bordering steps before it encounters another adatom to form an island. This is called the *step flow* growth mode, and it requires that the spacing l between steps is small compared to the spacing l_D between islands formed on a completely flat surface (the island spacing l_D is evident in Fig. 3a).

It is easy to determine the surface current (3) for a surface growing in step flow mode. Let us assume for simplicity that the step edge barrier is very strong, so that all adatoms have to attach to the upper step of a terrace. Then each adatom travels a mean distance $l/2$ between its point of arrival and the step, and the magnitude of the current is $Fl/2$. Since the surface height gradient is $|\nabla h| = a/l$, where a denotes the thickness of an atomic layer, we have that $f(m^2) = (F/2)a/m^2$ and

$$j(m) = \frac{Fa}{2m} \,. \tag{9}$$

Comparison with (8) shows that $\nu_{\parallel} > 0$ and $\nu_{\perp} < 0$, hence the current stabilizes the surface against step bunching but makes it unstable with respect to step meandering. While the first conclusion was reached already by Schwoebel and Shipsey [14] shortly after the discovery of the step edge barrier by Ehrlich and Hudda, the step meandering instability was predicted only much later, in 1990, by Bales and Zangwill [15]. Both these works relied on the model of step motion pioneered by Burton, Cabrera and Frank (BCF) [16], rather than on the continuum viewpoint presented here.

A detailed experimental study of growth-induced step meandering on copper surfaces vicinal to Cu(100) has been presented by Ernst and collaborators [17]; examples of the observed morphologies are shown in Fig. 5. The quantitative analysis of the patterns revealed, however, that the underlying mechanism in this case is *not* the one proposed by Bales and Zangwill. Instead, the meander is caused by the one-dimensional analogue of the Villain instability acting on the individual steps [18, 19, 20, 21]. The one-dimensional counterpart of the step edge barrier illustrated in Fig. 1 is an additional energy barrier which prevents atoms diffusing along a step edge from crossing kinks [22]. We will return to this issue below in Sect. 3.

2.2 Steering

In theories of epitaxial growth, it is usually assumed that the atoms arrive at the surface randomly and uniformly, without any dependence on the local surface morphology. The deposition flux could therefore be represented by a constant term F in (4). However, this assumption is not strictly true, because an atom approaching the surface feels the attractive force from the substrate atoms, which tends to deflect its trajectory away from a straight line. This effect is called *steering*, and it is well documented in molecular dynamics simulations [23, 24, 25]. The deflection becomes more pronounced the lower

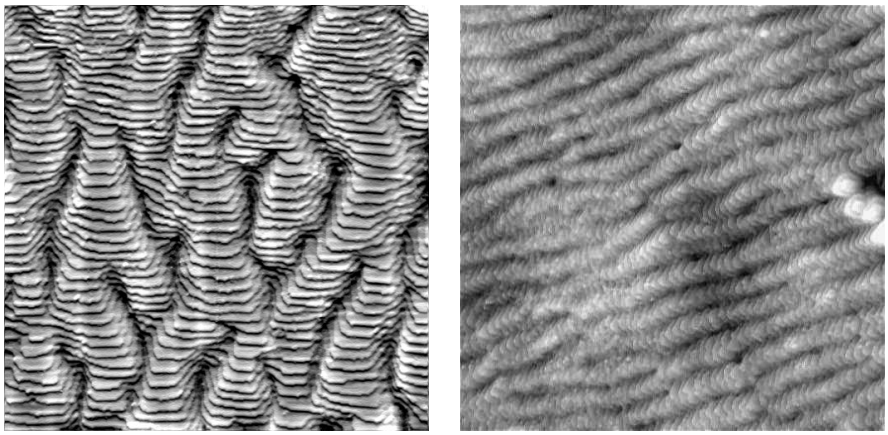

Fig. 5. Scanning tunneling microscope images of step meandering on copper surfaces vicinal to Cu(100) [17]. Left panel: Cu(1,1,17) surface after deposition of 18 ML of Cu at 280 K with flux $F = 5 \times 10^{-3}$ ML/s. The image size is 1000 Å $\times$ 1000 Å. Right panel: Cu(0,2,24) surface after deposition of 20 ML at 250 K with flux $F = 3 \times 10^{-3}$ ML/s; image size is 1300 Å $\times$ 1300 Å (from [17]). The mean step orientation is along the close–packed direction for the Cu(1,1,17) surface, and runs at 45° to the close–packed direction for the Cu(2,2,24) surface. Courtesy of Hans-Joachim Ernst

the kinetic energy of the incident atom, i.e., the lower the beam temperature. Experimentally, strong effects of steering have been observed in epitaxial growth of copper, when deposition occurs at near grazing incidence (the atom trajectories follow an angle of 80° from the surface normal) [26]. In this geometry steering implies an enhanced flux onto the top of islands near the ascending step, which leads to elongated island shapes and ripples. The same effect can be shown to induce step bunching on vicinal surfaces [25, 27].

Although steering affects the deposited atoms before they become adatoms, the consequences are rather similar to those of an uphill current along the surface, as it would be generated by a step edge barrier (Sect. 2.1) [25]. This idea was implemented already more than a decade ago in a simple one-dimensional growth model, where it leads to the formation of a morphology of well-separated columns [28].

In a continuum picture, in which morphological details such as steps and islands are ignored, the destabilizing effect of steering can be represented as in Fig. 6. There it is assumed that the trajectories are deflected abruptly towards the surface normal as soon as the atoms come within a distance δ from the surface. The flux that reaches a portion of the surface is then the flux that is incident on the "virtual surface" indicated by the dashed line in Fig. 6, which is obtained by moving the original surface by a distance δ along its normal. For a surface morphology with a typical radius of curvature R, this implies an excess flux of order $F(\delta/R)$ at the hilltops and a corresponding

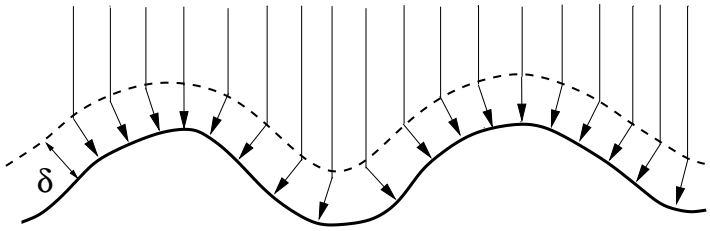

Fig. 6. Illustration of the destabilizing effect of steering during growth. In this simplified picture, it is assumed that depositing atoms follow straight vertical trajectories until they are within a distance δ from the surface, at which point they are abruptly deflected in the direction of the surface normal. It is evident that this implies a larger flux to hilltops than to valleys

reduction of the flux in the valleys. The flux becomes *curvature dependent* in a way that destabilizes the flat surface.

For a one-dimensional geometry, the effect can be described by the continuum equation

$$\frac{\partial h}{\partial t} = F - F\delta \frac{1}{[1 + (\partial h/\partial x)^2]^{3/2}} \frac{\partial^2 h}{\partial x^2} = F(1 + \delta\kappa), \tag{10}$$

where κ is precisely the curvature of the curve $h(x,t)$. Equation (10) was derived in [29, 30] based on the picture illustrated in Fig. 6, however with a different interpretation: The scale δ was taken to be the size of the deposited particles, and the instability was related to the columnar microstructure of thin films grown at low temperatures. For small deviations $\varepsilon(x,t)$ from the flat surface, (10) reduces to $\partial\varepsilon/\partial t = -F\delta\partial^2\varepsilon/\partial x^2$, and similarly in two dimensions $\partial\varepsilon/\partial t = -F\delta\nabla^2\varepsilon$, which is the same as (5) in the case of the Villain instability. A continuum equation with such a destabilizing term attributed to steering was proposed in [31] to describe the formation of mound-like structures in the growth of amorphous metal films.

2.3 Erosion by Ion Beams

It has been known for a long time that the erosion of a solid surface by ion bombardment gives rise to a variety of patterns such as pits and ripples [32, 33]. While much of the early results concerned amorphous solids, recent work has considered the erosion of single crystal metal surfaces [34, 35, 36, 37, 38, 39]. As an example, Fig. 7 shows the evolution of erosion pits during the bombardment of a Pt(111) surface with Xe^+ ions [34, 35]. The mechanism responsible for the formation of patterns like this will be described next, and we return to the case of amorphous surfaces in the second part of this subsection.

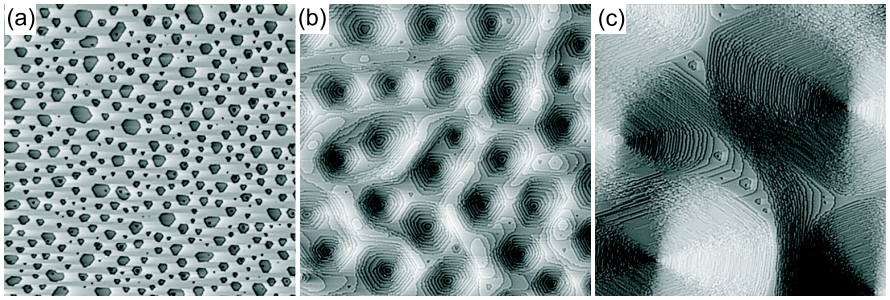

Fig. 7. Scanning tunneling microscope images of pit formation on Pt(111) by erosion with 1 keV Xe^+ ions at 650 K. The amount of removed material is (**a**) 0.26 ML, (**b**) 6.2 ML and (**c**) 454 ML. The topograph size is 1600 Å× 1610 Å. Courtesy of Thomas Michely

Erosion as Negative Growth

Evidently the shape of the pits seen in Fig. 7 is quite similar to an inverted version of the mounds in Fig. 3. Indeed, in the regime of interest here, the erosion process can be described in close analogy to epitaxial growth. To understand why this is so, we need to consider in some detail the atomic processes involved (see Fig. 8); this discussion is valid at not too low temperatures, above 20% – 30% of the melting temperature [35]. The net effect of an ion impact on the surface morphology is the creation of a few surface vacancies and adatoms. As these are created in close spatial vicinity, the recombination of vacancies and adatoms takes place rapidly, leaving a few excess surface vacancies behind to account for those atoms which have been sputtered away[3]. On intermediate time scales, ion bombardment can therefore be viewed as a process in which vacancies are "deposited" onto the surface.

Once created, the surface vacancies diffuse over the terrace, as sketched in Fig. 8b. When a vacancy encounters a descending step edge, it simply disappears. In contrast, at an ascending step edge, it can pass to the higher layer only if a step atom jumps into it. This requires not only that the step atom moves to the lower layer, which may be impeded by a step edge barrier, but it requires, first, that the step atom detaches from its lateral neighbors. A surface vacancy is therefore subject to an additional step edge barrier even when no such barrier exists for adatom diffusion [39]. This implies that the Villain instability should be generically present in ion beam erosion, and many of the concepts developed in Sect. 2.1 carry over to the erosion of crystalline

[3] It is also possible that the number of adatoms is larger than the number of surface vacancies, leading to net *growth* induced by ion bombardment, at the expense of the creation of bulk vacancies [40].

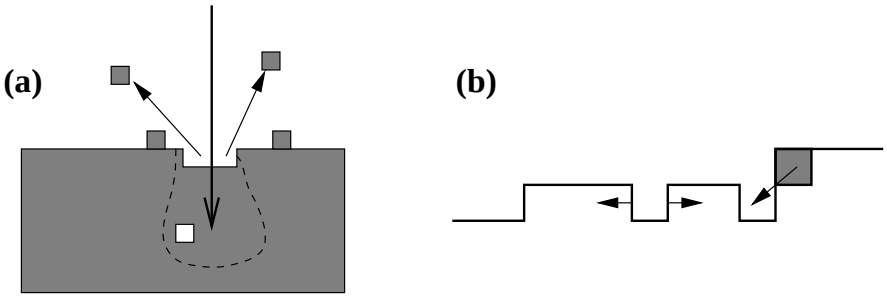

Fig. 8. Schematic of atomic processes in erosion. **(a)** An ion, indicated by the large arrow, penetrates into the solid and causes the material in the region enclosed by the dashed line to melt. After recrystallization of the melted region, the net effect of the ion impact is the creation of a bulk vacancy, three surface vacancies and two adatoms. Two atoms are sputtered away. **(b)** Intralayer and interlayer transport of surface vacancies. The surface vacancy on the right passes to the next higher layer when the shaded atom jumps into it

surfaces, however with the additional complication that one is dealing with currents of two diffusing species, adatoms and vacancies [35].

The Bradley-Harper Instability

A different mechanism for pattern formation by ion bombardment was proposed by Bradley and Harper to account for the numerous observations of sputter-induced ripple formation on amorphous surfaces [41]. The mechanism is based on a curvature dependence of the sputtering yield Y, the number of sputtered atoms per incident ion, and is, in this sense, similar to the growth instability due to steering discussed in Sect. 2.2. Within Sigmund's theory of sputtering [42], it is assumed that the energy deposited by the penetrating ion is distributed according to a Gaussian with an elliptic shape, and the sputtering yield is proportional to the deposited power density at the surface. As shown in Fig. 9, this implies a larger sputtering yield in the valleys than on the hilltops. A similar mechanism has been proposed to act on a macroscopic scale in abrasive waterjet cutting [43].

Starting from Sigmund's theory, Bradley and Harper computed the morphology dependence of the sputtering yield to linear order in the surface modulation. The ion beam is taken to impinge on the surface at an angle θ from the normal. For $\theta > 0$ the horizontal projection of the ion beam singles out a direction within the surface plane, which implies in-plane anisotropy in the topography evolution, similar to the case of growth on vicinal surfaces discussed in Sect. 2.1. Choosing the beam direction along the x-axis, the leading terms of the evolution equation read [41]

$$\frac{\partial h}{\partial t} = -Y_0(\theta) - \frac{\mathrm{d}Y_0}{\mathrm{d}\theta}\frac{\partial h}{\partial x} + \nu_{\parallel}(\theta)\frac{\partial^2 h}{\partial x^2} + \nu_{\perp}(\theta)\frac{\partial^2 h}{\partial y^2}. \tag{11}$$

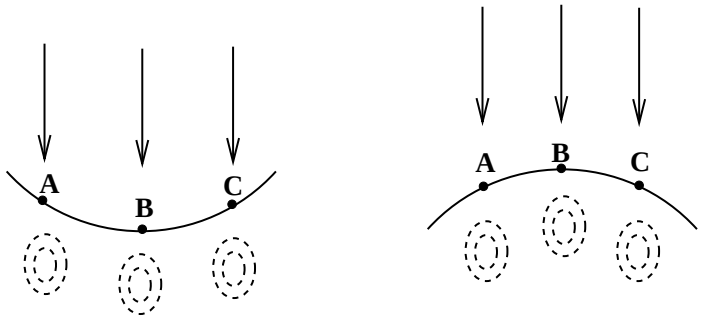

Fig. 9. Origin of the curvature dependence of the sputtering yield. Ions penetrating the surface at positions A, B and C deposit their energy as indicated by the dashed energy density contour lines. The energy deposited at B due to the ions incident at A and C is larger in **(a)** than in **(b)**, because the centers of the corresponding ellipses are closer to the surface point B. Therefore the sputtering yield is larger in a valley [**(a)**] than on a hilltop [**(b)**]

Here $Y_0(\theta)$ denotes the sputtering yield for a flat (unmodulated) surface. The second term on the right hand side describes the drift of surface features along the x-axis, while the stability of the flat surface is determined by the signs of the second derivative coefficients $\nu_{\parallel}$ and $\nu_{\perp}$ [compare to (7)]: An instability occurs when at least one of the two coefficients is negative, and the type of instability is determined by which of the negative coefficients is of larger absolute magnitude. Near normal incidence both coefficients are negative, as expected from Fig. 9, but near grazing incidence ($\theta \to 90°$) the instability along the beam direction is overcompensated by the fact that the (exposed) hilltops receive a larger ion flux than the valleys. Therefore $\nu_{\parallel} > 0$ and $\nu_{\perp} < 0$ for near-grazing incidence, which implies ripples running parallel to the beam direction. The ripple orientation rotates[4] at a critical angle θ_c, such that $\nu_{\parallel} < \nu_{\perp} < 0$ and the ripples run perpendicular to the beam direction for $\theta < \theta_c$. This scenario is well documented experimentally [32, 33, 44], and has also been observed in computer simulations [45].

2.4 Surface Electromigration

Surface electromigration is the biased motion of adatoms on the surface of a current–carrying solid. For metal surfaces, the dominant microscopic mechanism is the momentum transfer to the adatom caused by the scattering of conduction electrons (the *wind force*) [46, 47]; the direction of the electromigration force then coincides with the direction of electron flow. Much like

[4] In sputter erosion of crystalline surfaces, ripple rotation can also occur due to the crystalline anisotropy [37].

a flow of air or water causes the formation of ripples on a sand surface, the mass flow induced by electromigration can give rise to patterns on the surface of a solid [48]. Such patterns were first observed in 1938 on the surfaces of burned-out tungsten filaments in incandescent lamps [49]. Recent experimental studies on the morphological effects of surface electromigration on silicon have uncovered a whole zoo of patterns with a complicated temperature dependence [50], but the microscopic coupling between the electric current and the adatom motion is not clearly understood for this system.

A continuum description of the current-induced destabilization of a solid surface in a one-dimensional geometry was presented by Frohberg and Adam in 1975 [51]. Here we briefly describe the two-dimensional theory of [48], emphasizing the similarity to the growth instabilities discussed in Sect. 2.1, and show how simple considerations explain some features of the experimentally observed patterns. In the absence of growth and evaporation, the evolution equation for the surface is given by the conservation law (4) with $F = 0$. In contrast to the situation in Sect. 2.1, where the current $\boldsymbol{j}$ in (4) was induced by the deposition flux in conjuction with the step edge barrier, here the mass current along the surface is simply driven by the local electric field $\boldsymbol{E}$. Hence we can write

$$\boldsymbol{j} = \sigma(\nabla h) e Z^* \boldsymbol{E} \,, \tag{12}$$

where σ is the *adatom mobility*, e is the unit charge and Z^* denotes the effective valence of the adatom, which contains the details of the microscopic origin of the electromigration force. In the following we take $Z^* > 0$ without loss of generality.

The coupling between the electromigration current and the surface morphology arises because of the slope dependence of the mobility $\sigma(\nabla h)$. We expect that the mobility will be reduced in the presence of surface steps, which are able to trap the adatoms; the mobility should therefore be a decreasing function of $|\nabla h|$. Assuming isotropy in the plane, the mobility can then be expanded for small slopes in the form

$$\sigma(\nabla h) = \sigma_0 - \sigma_1 |\nabla h|^2 \tag{13}$$

with $\sigma_1 > 0$. Inserting (13) into (12) and (4), the stability of the general flat solution (2) with respect to a perturbation of the form (6) can be investigated.

The problem is similar to the stability analysis of the growing vicinal surface in Sect. 2.1, but it is more complicated because we are now faced with the interplay between *two* in-plane vectors, the tilt direction $\boldsymbol{m}$ and the electric field direction $\boldsymbol{E}$. This is reflected in the resulting expression for the growth rate of a perturbation with wavevector $\boldsymbol{q}$, which reads [48]

$$\omega(\boldsymbol{q}) = -2\sigma_1 (\boldsymbol{q} \cdot \boldsymbol{E})(\boldsymbol{q} \cdot \boldsymbol{m}). \tag{14}$$

Thus the surface is unstable against perturbations which satisfy the condition $(\boldsymbol{q} \cdot \boldsymbol{E})(\boldsymbol{q} \cdot \boldsymbol{m}) < 0$.

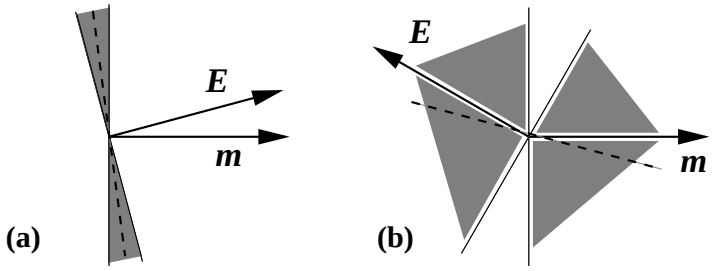

Fig. 10. Regions of unstable wavevectors (*shaded*) and most unstable direction (*dashed lines*) for the morphological instability caused by surface electromigration with different choices of the direction of the tilt vector $\boldsymbol{m}$ and the electric field vector $\boldsymbol{E}$

Most experiments on vicinal silicon surfaces have been limited to the situation where the electromigration force points either in the up-step direction ($\boldsymbol{E}$ and $\boldsymbol{m}$ parallel) or in the down-step direction ($\boldsymbol{E}$ and $\boldsymbol{m}$ antiparallel). The expression (14) implies stability for all $\boldsymbol{q}$ in the former case, and instability for all $\boldsymbol{q}$ in the latter. This is in agreement with the classic stability analysis carried out by Stoyanov within a one-dimensional step model based on BCF theory [52], which predicts a step-bunching instability when the force acts in the down-step direction (see [53] for a generalized treatment). For surfaces vicinal to Si(111), four different temperature regimes for electromigration-induced step bunching have been identified [50]. In each regime step bunching occurs either when the electric current is in the up-step or in the down-step direction, but the stable and unstable directions interchange when going from one regime to the next[5]. The step bunching mechanism first predicted by Stoyanov [52], and reproduced by the continuum theory [48], seems to be realized in the lowest temperature regime,

For general relative orientations of $\boldsymbol{E}$ and $\boldsymbol{m}$, the expression (14) implies that the stability depends on the direction of the perturbation wavevector $\boldsymbol{q}$ (Fig. 10). In particular, when $\boldsymbol{E}$ and $\boldsymbol{m}$ are almost, but not quite parallel, the unstable wavevectors accumulate in the direction *perpendicular* to $\boldsymbol{m}$ (Fig. 10a). As was discussed in Sect. 2.1, a perturbation wave vector perpendicular to $\boldsymbol{m}$, i.e., parallel to the steps, is indicative of a step meandering instability. Given that the local miscut typically displays some fluctuations relative to the global miscut $\boldsymbol{m}$, one may expect that step meandering persists also when the global miscut is exactly parallel to the field direction. Such a behavior has indeed been seen in Monte Carlo simulations [48].

The scenario is also qualitatively consistent with experimental observations for Si(111) in the second of the four temperature regimes mentioned

[5] The dependence of the stability of the surface on the current direction is a clear indication that a directional effect like electromigration must be involved, rather than just thermal effects related to Ohmic heating.

above, in which step meandering is found when the electric current is in the down-step direction and step bunching occurs for an up-step current [50]. Experiments carried out with other relative orientations of $\boldsymbol{E}$ and $\boldsymbol{m}$ near the down-step direction display patterns with wavevectors roughly between the vectors perpendicular to $\boldsymbol{E}$ and $\boldsymbol{m}$, as would be expected from (14) [54]. This interpretation of the experiments would imply, however, that the electromigration force is directed against the current in this temperature regime (i.e. that the effective valence Z^* in (12) is negative), which is known not to be the case from other measurements [55]. The actual mechanism acting in this temperature regime, as well as the origin of the additional transitions occuring at higher temperature, remains largely unexplained at present.

3 Wavelength Selection in the Linear Regime

When observing a regular array of ripples or mounds on a surface, the first, most obvious question to address concerns the origin of the characteristic length scale of the pattern. In the initial stages of the morphological instability, when the amplitude of modulation is small, this question can be answered on the basis of the linearized version of the evolution equation (1). The linear evolution equations derived in Sect. 2 do not select a characteristic wavelength, because they favor the growth of perturbations of arbitrarily small length scale: The growth rate $\omega(\boldsymbol{q})$ of the perturbation (6) is a quadratic function of $\boldsymbol{q}$, which grows without bounds as $|\boldsymbol{q}|$ increases.

Wavelength selection therefore requires that the instability mechanisms described in Sect. 2 are counteracted by a smoothening mechanism on short length scales, which reduces the growth rate $\omega(\boldsymbol{q})$ for large $|\boldsymbol{q}|$. Smoothening is generally driven by the increase of the surface free energy caused by the modulation. According to the Gibbs-Thomson relation, the chemical potential near a curved surface is enhanced by an amount $\Delta\mu = \gamma\kappa$, where γ is the surface free energy and κ is the curvature. The relaxation towards thermodynamic equilibrium thus drives a mass transfer from the maxima ($\Delta\mu > 0$) to the minima ($\Delta\mu < 0$) of the topography. The smoothening mechanism depends on the available kinetic pathways for mass transport, as was first analyzed by Mullins in a continuum setting [56]. For the conditions of interest here, the dominant smoothening mechanism is by surface diffusion. The surface diffusion current is proportional to the gradient of the chemical potential, and can thus be written in the form

$$\boldsymbol{j}_{\mathrm{smooth}} = -\sigma\nabla(\gamma\kappa) \approx K\nabla(\nabla^2)h, \tag{15}$$

where the small slope approximation $\kappa \approx -\nabla^2 h$ has been used, σ denotes the adatom mobility [compare to (12)] and $K = \sigma\gamma$.

We illustrate the wavelength selection mechanism using the Villain instability as an example. Adding the smoothening current (15) in the divergence

on the right hand side of (4) and linearizing around the horizontal, flat surface, we now obtain the equation

$$\frac{\partial \varepsilon}{\partial t} = -f(0)\nabla^2 \varepsilon - K(\nabla^2)^2 \varepsilon \ , \tag{16}$$

which leads to the wavenumber-dependent growth rate

$$\omega(\boldsymbol{q}) = f(0)|\boldsymbol{q}|^2 - K|\boldsymbol{q}|^4 \ . \tag{17}$$

This shows that the surface is stable ($\omega < 0$) against perturbations of wavenumbers $|\boldsymbol{q}| > q_c = \sqrt{f(0)/K}$, while the amplification is maximal for perturbations of wavenumber $q^* = q_c/\sqrt{2}$. The corresponding wavelength

$$\lambda^* = 2\pi/q^* = 2\pi\sqrt{2K/f(0)} \tag{18}$$

will therefore dominate the morphology in the early stages of growth. Analogous considerations apply to the other instabilities discussed in Sect. 2.

In order for (18) to attain predictive power, it is necessary to express the coefficients $f(0)$ and K in terms of microscopic quantities. This problem is discussed in detail elsewhere [4, 6, 57, 58]; here we only summarize the main results. When the step edge barrier is large, the initial length scale in mound growth is essentially determined by the spacing l_D of the submonolayer islands which form during the growth of the first layer, and which act as templates for the further evolution. This is the case in the growth experiment on Pt(111) shown in Fig. 3, and it is the typical behavior observed in metal homoepitaxy [4]. For weak barriers the continuum theory predicts that $\lambda^* \gg l_D$, and that mound formation is delayed such that the pattern appears only after the deposition of a large number of layers. This situation appears to be realized in homoepitaxial growth on Ge(100) [59, 60]. In this case the experimental measurement of the initial mound spacing can be used to infer quantitative information about the magnitude of the step edge barrier; at long times the mounds coarsen and steepen (see Sect. 4.1), which eventually leads to epitaxial breakdown (the formation of an amorphous film).

For the growth-induced step meandering instability on vicinal Cu(100) surfaces described in Sect. 2.1 (see Fig. 5), the quantitative analysis of the meander wavelength has been used to distinguish between two possible instability mechanisms, the Bales-Zangwill instability and the one-dimensional (1D) Villain instability [17, 20, 21]. As will be explained below in Sect. 4.1, in this case the meander wavelength does not change during growth, and therefore the experimentally observed wavelength of the fully developed pattern can be determined by linear stability analysis. For the Bales-Zangwill instability the meander wavelength $\lambda_\perp$ is predicted to scale with the deposition flux as $\lambda_\perp \sim F^{-1/2}$, while for the 1D Villain instability with strong kink rounding barriers the initial wavelength is set by the spacing between one-dimensional nuclei along the step, which scales as $F^{-1/4}$. The latter is consistent with

the experimentally observed flux dependence, while the former ist not [17]. Also the effective activation energy governing the temperature dependence of $\lambda_\perp$ is markedly different for the two mechanisms, because in the case of the Bales-Zangwill instability it involves energy barriers related to terrace diffusion and step crossing, whereas the 1D Villain instability is governed by step edge diffusion and kink crossing barriers. The assumption of the 1D Villain mechanism leads to a consistent description[6] of the experimental data, and allows (along with additional experimental information) to estimate the additional energy barrier for kink rounding [21, 22].

4 Scenarios of Nonlinear Evolution

Within the linearized theory, unstable modes grow exponentially according to (6). Thus after a time of order $\omega(q^*)^{-1}$ the modulation amplitude becomes so large that the nonlinear terms in the evolution equation can no longer be neglected. The nature of the subsequent evolution depends on the structure of these nonlinear terms. A priori, several different scenarios are conceivable: (i) The morphology may *coarsen*, in the sense that the characteristic wavelength increases with time. (ii) The topography may evolve at fixed local slope (*slope selection*) or it may *steepen* during evolution; steepening and coarsening may occur together, or steepening proceeds at fixed wavelength. (iii) Finally, the morphology may evolve in an irregular, *chaotic* fashion while locally retaining the characteristic wavelength of the linear regime. All these possibilities can be realized in the context of pattern formation at solid surfaces, and will be described in the following subsections.

4.1 Coarsening

In many cases coarsening involves a power law increase of the characteristic wavelength,

$$\lambda(t) \sim t^{1/z} , \tag{19}$$

which defines the *coarsening exponent* $1/z$. At the same time the modulation amplitude, measured e.g. through the surface width

$$w(t) = \sqrt{\langle (h - \bar{h})^2 \rangle} \tag{20}$$

also increases as

$$w(t) \sim t^{\beta} . \tag{21}$$

In (20), the angular brackets refer to a spatial average and $\bar{h}(t)$ is the mean height at time t. The exponent β in (21) is the *roughening exponent*. The

[6] This statement applies to the case when the average step orientation is along the close-packed direction (left panel of Fig. 5). The origin of the instability at the open steps (right panel of Fig. 5) is presently not well understood [21].

typical slope of the topography is of the order w/λ. Thus coarsening occurs at fixed slope if $\beta = 1/z$, while *steepening* occurs if $\beta > 1/z$. A special case is steepening at fixed lateral length scale, $1/z = 0$ and $\beta > 0$.

Coarsening is a familiar notion in the kinetics of first order phase transitions, where it refers to the evolution of the domain structure of the stable phases during phase separation [61]. Although we are here dealing with structures that do not, properly speaking, approach a state of thermal equilibrium, many of the concepts and methods developed in phase ordering kinetics can be, and have been, applied to kinetic surface instabilities [62, 63, 64, 65, 66, 67, 68]. Some of the pertinent results will be summarized below.

Coarsening of Mounds and Pits

The basic continuum model for the coarsening of mounds generated by the Villain instability can be constructed from the ingredients introduced in Sects. 2.1 and 3. We just need to specify the full slope dependence of the growth-induced current (3) and write it together with the smoothening current (15) on the right hand side of the evolution equation (4). The limiting behaviors of the function $f(m^2)$ for small and large slopes have been determined already: For $m \to 0$ it approaches a constant $f(0) > 0$, and for large m it vanishes as $1/m^2$ according to (9). A simple extrapolation formula which connects these two limits is [69]

$$f(m^2) = \frac{f(0)}{1 + (m/\hat{m})^2} \; ; \tag{22}$$

for a detailed justification and a discussion of the physical meaning of the parameters $f(0)$ and $\hat{m}$ we refer to [6, 57].

The form (9,22) implies that the uphill surface current remains nonzero for arbitrary values of the slope; as a consequence, the mounds steepen indefinitely. The mound slopes attain a finite limit only if $f(m^2)$ vanishes at some selected slope m^* [70, 71]. A simple functional form describing this situation is

$$f(m^2) = f(0)[1 - (m/m^*)^2]. \tag{23}$$

Once the current function $f(m^2)$ has been fixed, the full nonlinear evolution equation takes the form

$$\frac{\partial h}{\partial t} = -\nabla \cdot f(|\nabla h|^2)\nabla h - K(\nabla^2)^2 h + F \; . \tag{24}$$

To understand mathematically why the morphology described by (24) coarsens, it is useful to introduce the functional

$$\mathcal{L}[h(\boldsymbol{r},t)] = \int d\boldsymbol{r} \left(\frac{1}{2}(\nabla^2 h)^2 + \mathcal{V}(\nabla h) \right) \; , \tag{25}$$

where the *slope potential* $\mathcal{V}(\nabla h)$ is defined by

$$\mathcal{V}(\boldsymbol{m}) = -\frac{1}{2}\int_0^{|\boldsymbol{m}|^2} du\, f(u) \tag{26}$$

for an arbitrary choice of $f(m^2)$. Using the evolution equation (25), it is a simple matter to verify that [64, 65]

$$\frac{\mathrm{d}\mathcal{L}}{\mathrm{d}t} = -\int d\boldsymbol{r}\left(\frac{\partial h}{\partial t}\right)^2 < 0\,. \tag{27}$$

Thus $\mathcal{L}$ acts as an effective "free energy" functional for this nonequilibrium process, which is minimized during the evolution.

The two terms in the integrand of (25) describe different aspects of this minimization: On the one hand, the value of the slope potential $\mathcal{V}$ should be minimized locally; on the other hand, the square of the surface curvature $\nabla^2 h$ should become small. The minimization of the slope potential drives the process of slope selection. The potential has a minimum only if the function f goes through zero at some nonzero slope; otherwise, $\mathcal{V}$ decreases indefinitely with increasing $|\boldsymbol{m}|$, and the attempt to minimize it leads to unbounded steepening.

Within the continuum theory, the minimization of the surface curvature term in (25) provides the driving force for coarsening. The coarsening behavior therefore depends on how the curvature is distributed on the suface. In this respect the two models defined by (22) and (23) differ: For the model (22) without slope selection, the curvature is distributed evenly on the scale λ of the mounds, while for the model (23) with slope selection it is concentrated in the edges separating adjacent facets at which the selected slope $|\boldsymbol{m}| = m^*$ is attained. The width of these edge regions introduces an additional length into the problem, which invalidates naive dimensional analysis [61]. Based on these observations, scaling argument can be developed [4, 5] which show that the scaling exponents defined in (19,21) take the values $1/z = 1/4$, $\beta = 1/2$ for model (22) [62, 63] and $1/z = \beta = 1/3$ for model (23) [65]. For model (23) a weak version of the inequality $1/z \leq 1/3$ has been rigorously established [72].

Additional features of the model which may affect the coarsening exponents include in-plane anisotropy of the current function [which can then no longer be written in the form (3)] [19, 64, 65, 71, 73], fluctuations due to the shot noise in the deposition beam [74] and nonlinear terms which break the $h \to -h$ symmetry of the evolution equation (24). In the latter case one must distinguish between terms that also change the conserved nature of the evolution equation [75] and those that do not [67, 76]. Terms of the first kind lead to a significant speedup of coarsening, and will be discussed further in Sect. 4.3.

Experimentally, coarsening mound morphologies have been observed for a large number of homoepitaxial growth systems [4, 6]. The coarsening ex-

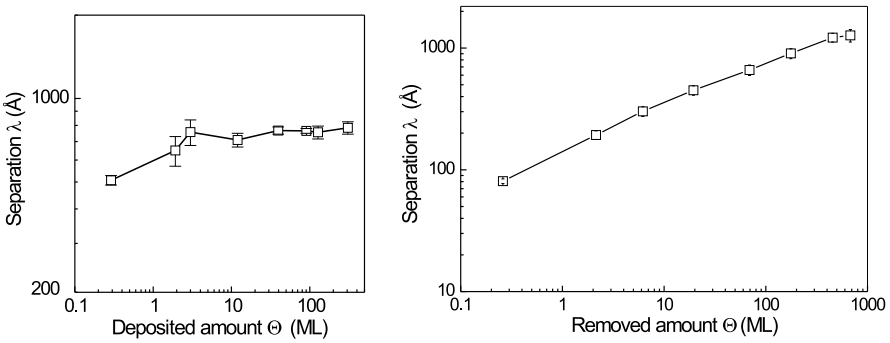

Fig. 11. Left panel: Evolution of the lateral mound separation, determined from the shape of the height-height correlation function, during growth of Pt on Pt(111) at 440 K. Right panel: Evolution of the lateral pit size during ion erosion of Pt(111) at 650 K. Courtesy of Thomas Michely

ponents typically fall into the range $1/6 \leq 1/z \leq 1/3$. The growth of Pt on Pt(111) is an exception: As is seen in Fig. 3 and demonstrated quantitatively in Fig. 11, for this system the mound morphology evolves at constant lateral length scale. At the same time the surface roughness increases with the square root of the deposit thickness, leading to the scaling exponents $1/z = 0$ and $\beta = 1/2$ [11]. This behavior can be well described by a simple model for the growth of a single mound which does not exchange mass with its neighbors [4, 5, 77, 78]. The model provides a detailed prediction for the shape of the individual mounds, which can be used to infer the value of the step edge barrier [79].

In contrast to the growth at 440 K, the pit morphology formed during ion erosion of Pt(111) at 650 K clearly coarsens, with a coarsening exponent of $1/z = 0.30 \pm 0.02$ [34, 35] (see Figs. 7 and 11). This difference in behavior shows that the microscopic mass transport process needed for coarsening, the generation of step adatoms at kinks, becomes thermally activated between 440 and 650 K [4, 80]. Coarsening of surface structures formed by ion erosion has also been reported for pits on Au(111) [36] and ripples on Cu(110) [38].

Coarsening in One Dimension

A detailed mathematical analysis of coarsening is possible for one-dimensional evolution equations. In one dimension, the growth equation (24) with the current function (23) becomes equivalent to the Cahn-Hilliard equation of phase ordering kinetics [61]. For this system it was shown long ago by Langer that the domain size grows logarithmically, $\lambda \sim \ln t$ [81]. Langers derivation is based on the analysis of the stationary periodic solutions of the equation. These periodic solutions are all linearly unstable, but the characteristic lifetime on which they decay increases exponentially with the wavelength, reflecting the exponential spatial decay of the interactions between the domain

walls. During coarsening the system passes through a sequence of almost periodic configurations, and the time it spends in each is given by the lifetime of the corresponding stationary solution. Inverting the relationship between the lifetime and the wavelength thus yields the coarsening law.

Politi and Torcini have applied this approach to the one-dimensional version of the surface evolution equation (24) with a generalization of the current function (22), in which the current decays for large slopes as $j(m) \sim |m|^{-\gamma}$, with $\gamma \geq 1$ [68]. They find that $1/z = 1/4$ for $1 \leq \gamma \leq 3$ and $1/z = (1+\gamma)/(1+5\gamma)$ for $\gamma > 3$. This is in contrast to the scaling arguments employed in the two-dimensional case, which would predict that $1/z = 1/4$ independent of γ. The reason for the discrepancy is that the different, competing contributions which govern the growth of λ and w, and which are assumed in the scaling theory to be of a similar order of magnitude, may precisely cancel, to leading order, in the one-dimensional case [6]. As a consequence, the scaling arguments only give an upper bound on the coarsening exponent.

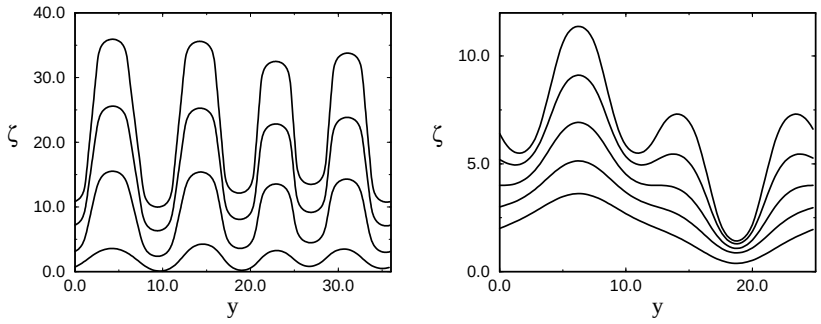

Fig. 12. Left panel: Time evolution of the collective step meander according to (28) with $\mu = 1/2$. Right panel: When the evolution equation (28) is started with an initial condition of wavelength $\lambda_0 > 2\lambda^*$, an additional meander appears; here $\lambda_0 = 2.8\lambda^*$

One-dimensional growth equations appear naturally in the description of the nonlinear evolution of vicinal surfaces undergoing the Bales-Zangwill instability [82, 83, 84]. The linear stability analysis shows that the different steps meander in phase in the early time regime [85]; within the continuum theory of Sect. 2.1, this is reflected in the fact that, because $\nu_{\|} > 0$ and $\nu_{\perp} < 0$, the growth rate $\omega(\boldsymbol{q})$ is maximal for perturbations with $q_x = 0$. Therefore a single, one-dimensional function $x = \zeta(y,t)$ is sufficient to describe the displacement of the common step profile from the flat straight reference configuration $\zeta = 0$. A solvability condition arising from a multiscale expansion of the BCF equations for the problem yields an evolution

equation of the form [84]

$$\zeta_t = -\left\{ \frac{A\,\zeta_y}{1+\zeta_y^2} + \frac{B}{(1+\zeta_y^2)^{\mu}} \left[\frac{\zeta_{yy}}{(1+\zeta_y^2)^{3/2}} \right]_y \right\}_y , \tag{28}$$

where subscripts denote partial derivatives and A and B are positive constants. The first term inside the curly brackets is destabilizing and proportional to the deposition flux, while the second term is a one-dimensional version of the stabilizing smoothening current introduced in (15). The expression inside the square brackets is the curvature of the step, and the term multiplying the square brackets is a kind of mobility, which depends on the dominant channel for mass transport; the exponent $\mu = 1$ when mass transport is over the terraces (the coefficient B is then proportional to the adatom diffusion coefficient on the terrace), and $\mu = 1/2$ when mass transport is along the step (with B proportional to the step edge diffusion coefficient) [83]. The geometric nonlinearities in (28) arise because, in contrast to (15), here the shape gradient ζ_y is not assumed to be small.

For the physically relevant values of μ (more precisely, for $\mu > -1/2$) the step patterns generated by (28) show an unbounded growth of the meander amplitude as $\sqrt{t}$, but no lateral coarsening (Fig. 12). This finding is consistent with the experimental observation that the wavelength of the step meander does not change during growth [17]. Asymptotically for large t, the equation admits separable solutions of the form $\zeta(y,t) = \sqrt{t}\, g(y)$, where the function $g(y)$ can be constructed to have *any* wavelength larger than a minimal value $\lambda_{\min}$. Starting from an initial condition with small random fluctuations, the wavelength of the pattern is determined by the maximum of the linear growth rate, as explained in Sect. 3. In the notation of (28), the maximally unstable wavelength is $\lambda^* = 2\pi\sqrt{2B/A}$, and $\lambda^* > \lambda_{\min}$ for $\mu > 0.2283$. Patterns with wavelengths larger than λ^* can be created by starting with an appropriate initial condition; however the initially chosen wavelength λ_0 persists only up to $\lambda_0 \approx 2\lambda^*$, as for larger values an additional meander can grow between the maxima and minima of the initial profile (Fig. 12).

In general, the presence or absence of coarsening for an evolution equation like (28) depends on the relationship between the wavelength λ and the amplitude $\mathcal{A}$ of its periodic stationary solutions: Coarsening requires that $\mathrm{d}\lambda/\mathrm{d}\mathcal{A} > 0$ [86]. This condition is satisfied in (28) for arbitrarily large λ when $\mu < -1/2$ [83]. A physical mechanism which changes the form of the nonlinearities in (28) such as to induce coarsening is the elastic interaction between steps [87]. Somewhat surprisingly, it is not obvious whether a one-dimensional surface evolution equation with stationary, fixed wavelength solutions which neither coarsen nor steepen can be written down [86]; this question is of interest in relation to sand ripples formed under an oscillatory flow of water [88].

Coarsening and Scaling of Step Bunches

A clear experimental example for power law coarsening is provided by the electromigration-induced step bunching of Si(111), where the distance L between step bunches is found to increase with time as $L \sim t^{1/2}$ in two of the temperature regimes mentioned in Sect. 2.4 [89]. This behavior has been reproduced in Monte Carlo simulations [48] as well as in a step-dynamical model based on BCF theory [90, 91]. In addition, the scaling relations

$$N \sim W^{\alpha}, \quad l_{\min} \sim N^{-\gamma} \tag{29}$$

connecting the number of steps in a bunch, N, the minimal distance between steps in the bunch, $l_{\min}$, and the lateral width W of the bunch have been proposed [90, 92, 91] and experimentally verified [93]. The minimal step distance decreases with increasing N, because in a large bunch the steps are pushed more strongly together against the repulsive step-step interaction. Depending on the temperature regime, the values $\gamma = 0.60 \pm 0.04$ and $\gamma = 0.68 \pm 0.03$ were obtained experimentally for Si(111) [93].

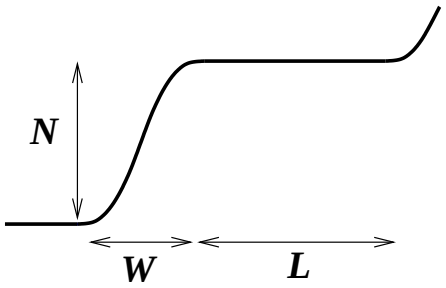

Fig. 13. Characteristic length scales of a step bunch

In order of magnitude, $l_{\min} \sim W/N$, which yields the exponent identity $\gamma = 1 - 1/\alpha$. The steepening of the bunch with increasing size implies $\gamma > 0$ and hence $\alpha > 1$. Since the overall surface slope is fixed globally, we also have $L \sim N$. It is important to note that W and L define two distinct lateral length scales characterizing the bunch morphology (see Fig. 13). Introducing a coarsening exponent $1/z$ through $W \sim t^{1/z}$, it follows that $L \sim t^{\alpha/z}$, which grows faster than W when $\alpha > 1$.

A unified framework for describing the scaling properties of step bunch morphologies has recently been proposed by Pimpinelli and coworkers [94]. It is based on the continuum equation

$$\frac{\partial h}{\partial t} = -\frac{\partial}{\partial x} j(m) - K \frac{\partial}{\partial x} |m|^{-k} \frac{\partial^2}{\partial x^2} |m|^{n} \tag{30}$$

for the one-dimensional surface profile $h(x,t)$ perpendicular to the steps (in the x-direction, see Fig. 4). Here $m = \partial h/\partial x$ is the slope in the x-direction[7], $j(m)$ is the destabilizing surface current, and the second term on the right hand side describes the smoothening of the vicinal surface by surface diffusion, with $K > 0$ being proportional to the surface diffusion coefficient. For a vicinal surface, the driving force for smoothening is the repulsive interaction between the surface steps. The step-step repulsion is encoded in the exponent n, which describes the decay of the interaction potential with step distance l as l^{-n}; for the most common type of entropic and elastic step-step interactions, $n = 2$ [7]. The exponent k in (30) is related to the diffusion kinetics on the vicinal surface[8]. If diffusion on the terraces is fast compared to the attachment-detachment processes at the steps we have $k = 1$, while in the opposite limit $k = 0$ [95, 96].

In addition, it is assumed in [94] that the destabilizing current $j(m)$ can be represented by its leading order term in a gradient expansion, $j(m) \approx Bm^{\rho}$, where $B\rho > 0$ to satisfy the condition $\mathrm{d}j/\mathrm{d}m > 0$ required for a linear instability (compare to Sect. 2.1). Then the scaling exponents α and z can be determined by requiring that (30) should be invariant under the scale transformation

$$h(x,t) \;\Rightarrow\; b^{-\alpha} h(bx, b^z t) \tag{31}$$

for an arbitrary scale factor b. Comparing the three terms on the right hand side of (30) yields two conditions for the unknown exponents α and z, which are solved by the expressions

$$\alpha = 1 + \frac{2}{n-k-\rho}, \quad \gamma = \frac{2}{2+n-k-\rho}, \quad z = \frac{2(1+n-k-2\rho)}{n-k-\rho}\,. \tag{32}$$

The authors of [94] argue that all known examples of step bunching are covered by three *universality classes* corresponding to $\rho = 1$, $\rho = -1$ and $\rho = -2$.

Let us see how this framework applies to the problem of electromigration-induced step bunching. For detachment-limited dynamics, a continuum equation can be derived which has the form (30) with $\rho = -1$ and $k = 1$ [90]. According to (32), this implies $\gamma = 2/(2+n)$, in particular $\gamma = 1/2$ for the canonical case $n = 2$. This result is at variance with numerical simulations of step dynamical models [91, 92], which yield $\gamma = 2/(1+n)$, as well as with the experimental results quoted above [93], which are consistent with $\gamma = 2/3$.

The reason for the discrepancy is revealed by a careful analysis of the stationary solutions of (30) [97]. The shape of a stationary bunch is obtained by setting the total current on the right hand side of (30) equal to a constant j_0. As explained in [90], this current must be determined by the microscopic boundary conditions at the step, and it turns out to be *independent* of the

[7] We take $m > 0$ without loss of generality.

[8] In [94], only the case $k = 0$ was considered.

bunch size. As the bunches steepen with increasing size, this implies that the destabilizing current $j(m) \sim 1/m$ becomes *irrelevant* relative to the mean current j_0 for large bunches. Their shape is instead determined by the balance between j_0 and the stabilizing term. In this sense the correct value of ρ to chose for the scaling of the stationary bunch shape is $\rho = 0$. Together with $k = 1$ this gives $\gamma = 2/(1+n)$, in agreement with simulations [92, 91] and experiments [93].

Turning next to the dynamic scaling properties, we have already noted that experiments on Si(111) yield $\alpha/z = 1/2$ [89]. Step dynamical simulations show that this result is actually independent[9] of the step interaction exponent n [91]. Inspection of the expressions (32) reveals that $\alpha/z = 1/2$ independent of n only if $\rho = -1$. Thus, as far as the dynamical properties are concerned, our initial, naive choice $\rho = -1$ is appropriate. This probably reflects the fact that the coarsening dynamics is governed by current differences, which are not affected by the mean current j_0.

While somewhat preliminary and incomplete, the considerations in this subsection show that the step bunch equation (30) must be interpreted with caution. It must be kept in mind that the derivation of a continuum equation from discrete step dynamics can be rigorously justified [98] only when the terrace size is a slowly varying function of the terrace index. This condition clearly breaks down at the boundaries of the step bunch, where the steeply sloped part joins the large terraces that separate it from neighboring bunches.

4.2 Chaotic Bubbling

Coarsening is the typical long-time behavior for surface evolution equations that are of conservation type, in the sense that the terms on the right hand side can be written (apart from an additive constant) as the divergence of a mass current. The Villain instability in epitaxial growth and the instabilities related to surface electromigration (in the absence of desorption) fall into this class of *conserved* dynamics, but the steering instability and the Bradley-Harper instability in ion erosion of amorphous surfaces do not. As a representative example of the class of *non-conserved* surface dynamics, we discuss here the nonlinear evolution of the Bradley-Harper instability.

Building on the work of Bradley and Harper [41] and of Sigmund [42], Cuerno and Barabási derived the leading order nonlinear contributions in the expansion of the sputtering yield Y in terms of the gradients of the topography [33, 99]. The resulting evolution equation is of the form

$$\frac{\partial h}{\partial t} = \nu_{\parallel}\frac{\partial^2 h}{\partial x^2} + \nu_{\perp}\frac{\partial^2 h}{\partial y^2} + \frac{\lambda_{\parallel}}{2}\left(\frac{\partial h}{\partial x}\right)^2 + \frac{\lambda_{\perp}}{2}\left(\frac{\partial h}{\partial y}\right)^2 - K(\nabla^2)^2 \,, \qquad (33)$$

[9] An appealing explanation for the robustness of the value 1/2 for the coarsening exponent is given in [90]; the argument assumes, however, that the bunch spacing L is the only lateral length scale in the problem, which is not strictly true.

where the first two terms on the right hand side of (11) have been eliminated by going to a comoving frame, and the smoothening current (15) has also been added. Clearly the nonlinear terms $\sim (\partial h/\partial x)^2$, $(\partial h/\partial y)^2$ cannot be written as the divergence of a conserved current.

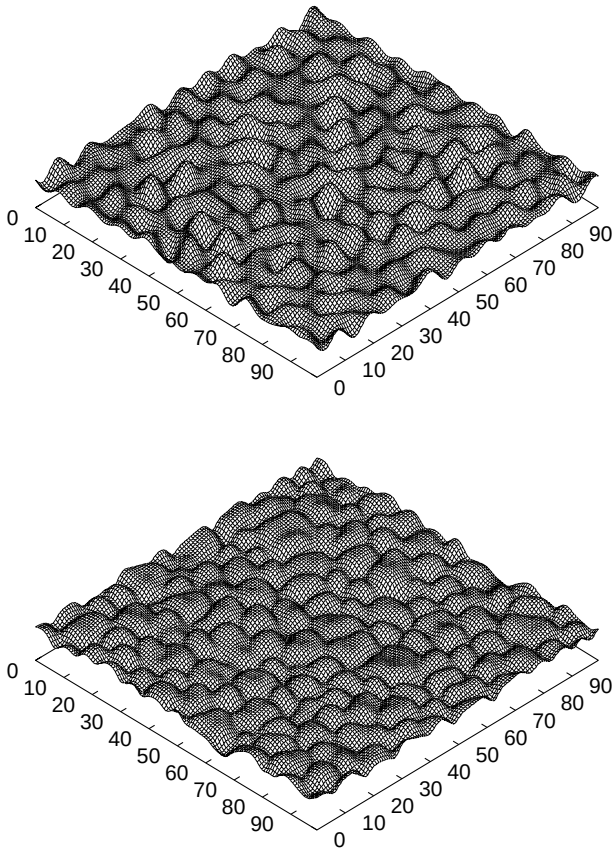

Fig. 14. Snapshots from the evolution of the isotropic, two-dimensional Kuramoto-Sivashinsky equation. The upper panel shows the early time regime governed by the linear instability, the lower panel shows the fully developed chaotic state. Note that the lateral length scale is the same in both images, but in the chaotic regime a cellular structure with clear up-down asymmetry has developed. Courtesy of Martin Rost

Equation (33) is an anisotropic, two-dimensional generalization [100] of the *Kuramoto-Sivashinsky* (KS) equation, which was originally derived in the context of flame front propagation [101] and phase dynamics in spatially extended oscillatory systems [102]. The KS equation has become a paradigm of *spatio-temporal chaos* [103, 104]. It is the prime example of an interface

evolution equation where the nonlinear terms stabilize the linear instability not by forcing the system into a near-periodic morphology which evolves more and more slowly through coarsening, but instead by establishing a dynamic steady state of irregular but bounded fluctuations. Two snapshots from the evolution of the isotropic, two-dimensional KS equation are shown in Fig. 14. The surface consists of convex cells of a characteristic size given by the most unstable wavelength λ^* of the linear instability (see Sect. 3). These cells split and merge in a random fashion, leading to an appearance of chaotic bubbling[10], similar, perhaps, to the surface of a boiling mudpool. On large length scales, the chaotic fluctuations can be described by an effective stochastic interface equation [105, 106, 107].

The introduction of anisotropy [100] opens up the possibility of qualitatively different modes of evolution, apart from the isotropic chaotic state shown in Fig. 14. For example, when $\nu_\parallel > 0$ and $\nu_\perp < 0$, as in the Bradley-Harper instability at near grazing ion beam incidence, and $\lambda_\parallel$ and $\lambda_\perp$ have the same sign, then the initial pattern of ripples parallel to the x-axis undergoes a secondary pinching instability, and the surface develops an anisotropic chaotic pattern with a finite coherence length along the ripples. The most dramatic anisotropy effect occurs when $\lambda_\parallel/\lambda_\perp < 0$ and $\nu_\parallel/\nu_\perp > \lambda_\parallel/\lambda_\perp$ (with at least one of the two linear coefficients $\nu_{\parallel,\perp}$ negative). Then (33) can be shown to possess one-dimensionally modulated solutions for which the nonlinear terms precisely cancel, and which therefore show unbounded exponential growth. These *cancellation modes* correspond to tilted ripple patterns in which the ripples form an angle $\pm \arctan\sqrt{-\lambda_\parallel/\lambda_\perp}$ with respect to the y-axis. Because the angle can take two different values, there are actually two symmetry-related ripple patterns which compete for domination of the surface. As a consequence, a kind of coarsening scenario is observed which seems to prevent the exponential blowup of the modulation amplitude. This remarkable prediction of the continuum theory has so far not been verified experimentally, but it has been shown numerically that the phenomenon persists in the presence of external noise [108].

4.3 From Coarsening to Chaos

Having described two qualitatively different scenarios for nonlinear morphological evolution in the preceding two subsections 4.1 and 4.2, we now ask how the transition from one regime to the other occurs when, for example, the height conservation property of the evolution equation is only weakly violated. A physically relevant example is epitaxial growth in the presence of a small amount of desorption. A continuum description of this situation is provided by the evolution equation[11] [75]

[10] This term was suggested to me by Per Jögi.

[11] Similar equations have been used to describe the faceting of thermodynamically unstable surfaces in the presence of a growth flux [109, 110].

$$\frac{\partial h}{\partial t} = -\nabla \cdot [1 - (\nabla h)^2]\nabla h - (\nabla^2)^2 h + F - \frac{\varrho}{1 + (\nabla h)^2} \,, \tag{34}$$

which combines the (suitably rescaled) mound evolution equation (24) [with slope selection, i.e. $f(m)$ given by (23)] with an additional nonlinear term modeling the desorption flux. The form of this term can be motivated from BCF theory. Qualitatively, it expresses the fact that the desorption flux decreases with increasing tilt (increasing step density), because the atoms are captured by steps before they can desorb; the coefficient ϱ in (34) is proportional to the desorption rate on a flat terrace.

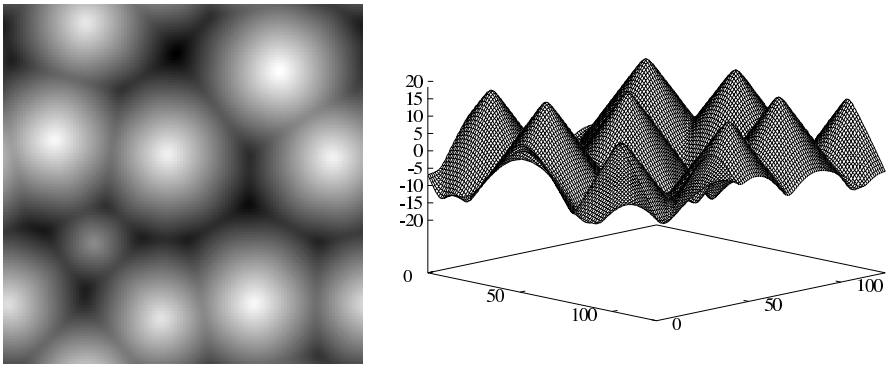

Fig. 15. Mounded surface generated by the evolution equation (34) with $\varrho \approx 0.32$. Conical mounds (right) form a cellular structure shown in gray-scale representation on the left

The desorption term breaks the up-down symmetry of the evolution equation (24) and leads to a morphology of conical mounds (Fig. 15). More importantly, desorption is found to significantly speed up the coarsening behavior, with the coarsening exponent increasing from $1/z = 1/3$ for $\varrho = 0$ (see Sect. 4.1) to $1/z = 1/2$ for $\varrho \neq 0$ and long times [75]. This result can be understood as follows. Desorption occurs mostly from flat surface regions, i.e. from hilltops and valleys. Because of the up-down asymmetry, hilltops are pointlike whereas valleys form a network of lines. The fraction of the surface occupied by valleys is of order $1/\lambda$, much larger than the fraction $\sim 1/\lambda^2$ occupied by hilltops. As more material desorbs from the valleys than from the hilltops, the peak-to-valley height difference grows at rate ϱ/λ. Due to the slope selection property of the evolution equation, the lateral mound size has to increase at the same rate. Thus we have

$$\mathrm{d}\lambda/\mathrm{d}t \approx \varrho/\lambda \quad \Rightarrow \quad \lambda \approx \sqrt{\varrho t} \,. \tag{35}$$

A model system for which the speedup of coarsening and the transition from coarsening to chaotic dynamics has been studied in detail is the one-dimensional *convective Cahn-Hilliard equation* [110, 111]

$$\frac{\partial m}{\partial t} + \frac{\partial^2}{\partial x^2}(m - m^3) + \frac{\partial^4 m}{\partial x^4} + 2\varrho m \frac{\partial m}{\partial x} = 0 \,. \tag{36}$$

This is just the one-dimensional version of (34), written in terms of the slope $m = \partial h/\partial x$, in which the desorption term has been replaced by its leading gradient expansion. For $\varrho = 0$ (36) becomes the one-dimensional Cahn-Hilliard equation [61], which shows logarithmic coarsening, as was mentioned above in Sect. 4.1. The term proportional to ϱ has a formal similarity with the nonlinear convection term in the equations of hydrodynamics; it implies that fluctuations in m are convected at a speed proportional to m. Equation (36) has been introduced as a description of phase ordering kinetics in the presence of an external field [112, 113] and in the context of step growth with crystal anisotropy [114].

Rewriting (36) in terms of the rescaled variable $\tilde{m} = \varrho m$ and taking $\varrho \to \infty$, one finds that (36) reduces to the one-dimensional KS equation, which displays spatio-temporal chaos (see Sect. 4.2). Thus it is clear that (36) must show a transition from coarsening to chaos as ϱ is increased. The analysis of the stationary ($\partial m/\partial t = 0$) solutions of (36) indeed shows that weakly unstable periodic patterns, through which the coarsening process passes, exist only for $2\varrho < \sqrt{2}/3$. For larger values of ϱ stationary and traveling wave solutions with a fixed periodicity and amplitude are found, while around $2\varrho \approx 7$ spatio-temporal chaos sets in [110].

The coarsening behavior of (36) for small but nonzero ϱ has been analyzed in [111]. In this work the phenomenologically derived [113] scaling law (35) has been firmly established for times $1/\varrho \ll t \ll 1/\varrho^3$. For even longer times a crossover to logarithmic coarsening, as in the standard Cahn-Hilliard equation, is found.

5 Conclusion

An important lesson from the examples described in this article is that similar patterns can be formed through widely different mechanisms. For solid surfaces driven out of equilibrium, patterns of mounds or pits typically appear if no in-plane direction is distinguished, while in the presence of a direction singled out by, e.g., the surface miscut, an electric current or an erosion beam, ripples perpendicular or parallel to this direction can be expected. The existence of a small number of archetypical patterns implies that the appearance of a particular pattern on a surface does not tell us much about the processes that are involved in its formation.

We should therefore be cautious in postulating analogies between widely different systems just on the basis of qualitative similarities in the observed

patterns; this applies even more when patterns on the nanometer scale are compared to macroscopic patterns like sand ripples and dunes (although in some cases such an analogy can be well-founded, see [48]). It is only through a detailed quantitative analysis of the microscopic physics, in close cooperation between theory and experiment, that an understanding of the mechanisms responsible for pattern formation, and thus, the ability to manipulate the features of the patterns can be achieved. In this article I have described some of the recent progress in this direction; but clearly much work remains to be done.

Acknowledgements

The work on continuum equations began in collaboration with Michael Plischke and Martin Siegert, and continued with Claudio Castellano, Harvey Dobbs, Jouni Kallunki, Miroslav Kotrla, Paolo Politi, Martin Rost and Pavel Šmilauer. I am most grateful to Thomas Michely for many enlightening discussions and a critical reading of the manuscript, and I thank him as well as Hans-Joachim Ernst and Martin Rost for providing figures. Stoyan Stoyanov has promoted my understanding of electromigration-induced step bunching. Financial support has been provided by DFG within SFB 237 *Unordnung und grosse Fluktuationen* and SFB 616 *Energiedissipation an Oberflächen*, and by Volkswagenstiftung.

References

1. M.C. Cross, P.C. Hohenberg: Rev. Mod. Phys. **65**, 851 (1993)
2. J.L. Hansen, M. van Hecke, C. Ellegaard, K.H. Andersen, T. Bohr, A. Haaning, T. Sams: Phys. Rev. Lett. **87**, 204301 (2001)
3. K.H. Andersen, M. Abel, J. Krug, C. Ellegaard, L.R. Søndergaard, J. Udesen: Phys. Rev. Lett. **88**, 234302 (2002)
4. T. Michely, J. Krug: *Islands, Mounds and Atoms. Patterns and Processes in Crystal Growth Far From Equilibrium* (Springer, Berlin 2003)
5. J. Krug: Physica A **313**, 47 (2002)
6. P. Politi, G. Grenet, A. Marty, A. Ponchet, J. Villain: Phys. Rep. **324**, 271 (2000)
7. A. Pimpinelli, J. Villain: *Physics of Crystal Growth* (Cambridge University Press, Cambridge 1998)
8. C. Teichert: Phys. Rep. **365**, 335 (2002)
9. G. Ehrlich, F. Hudda: J. Chem. Phys. **44**, 1039 (1966)
10. J. Villain: J. Phys. I France **1**, 19 (1991)
11. M. Kalff, P. Šmilauer, G. Comsa, T. Michely: Surf. Sci. **426**, L447 (1999)
12. J. Krug, M. Schimschak: J. Phys. I **5**, 1065 (1995)
13. M. Rost, P. Šmilauer, J. Krug: Surf. Sci. **369**, 393 (1996)
14. R.L. Schwoebel, E.J. Shipsey: J. Appl. Phys. **37**, 3682 (1966)
15. G. S. Bales, A. Zangwill: Phys. Rev. B **41**, 5500 (1990)

16. W. Burton, N. Carbrera, F. C. Frank: Phil. Trans. Roy. Soc. A **243**, 299 (1951)
17. T. Maroutian, L. Douillard, H.-J. Ernst: Phys. Rev. B **64**, 165401 (2001)
18. O. Pierre-Louis, M. R. D'Orsogna, T. Einstein: Phys. Rev. Lett. **82**, 3661 (1999)
19. P. Politi, J. Krug: Surf. Sci. **446**, 89 (2000)
20. M. Rusanen, I. T. Koponen, J. Heinonen, T. Ala-Nissila: Phys. Rev. Lett. **86**, 5317 (2001)
21. J. Kallunki, J. Krug, M. Kotrla: Phys. Rev. B **6**5, 205411 (2002)
22. J. Kallunki, J. Krug: Surf. Sci. Lett. **523**, L53 (2003)
23. D.E. Sanders, D.M. Halstead, A.E. DePristo: J. Vac. Sci. Technol. A **10**, 1986 (1992)
24. F. Montalenti, A.F. Voter: Phys. Rev. B **64**, 081401 (2001)
25. J. Yu, J.G. Amar: Phys. Rev. Lett. **89**, 286103 (2002)
26. S. van Dijken, L.C. Jorritsma, B. Poelsema: Phys. Rev. B **61**, 14047 (2000)
27. J. Krug (unpublished)
28. H. Park, A. Provata, S. Redner: J. Phys. A **24**, L1391 (1991)
29. A. Mazor, D.J. Srolovitz, P.S. Hagan, B.G. Bukiet: Phys. Rev. Lett. **60**, 424 (1988)
30. D.J. Srolovitz, A. Mazor, B.G. Bukiet: J. Vac. Sci. Technol. A **6**, 2371 (1988)
31. M. Raible, S.G. Mayr, S.J. Linz, M. Moske, P. Hänggi, K. Samwer: Europhys. Lett. **50**, 61 (2000)
32. G. Carter, B. Navinšek, J.L. Whitton: 'Heavy Ion Sputtering Induced Surface Topography Development'. In: *Sputtering by Particle Bombardment I*, Topics in Applied Physics Vol. 47, ed. by R. Behrisch (Springer, Berlin 1981) pp. 231–269
33. M.A. Makeev, R. Cuerno, A.-L. Barabási: Nucl. Instr. and Meth. B **197**, 185 (2002)
34. T. Michely, M. Kalff, G. Comsa, M. Strobel, K.-H. Heinig: Phys. Rev. Lett. **86**, 2589 (2001)
35. M. Kalff, G. Comsa, T. Michely: Surf. Sci. **486**, 103 (2001)
36. M.V.R. Murty, T. Curcic, A. Judy, B.H. Cooper, A.R. Woll, J.D. Brock, S. Kycia, R.L. Headrick: Phys. Rev. Lett. **80**, 4713 (1998)
37. S. Rusponi, G. Costantini, C. Boragno, U. Valbusa: Phys. Rev. Lett. **81**, 2735 (1998)
38. S. Rusponi, G. Costantini, C. Boragno, U. Valbusa: Phys. Rev. Lett. **81**, 4184 (1998)
39. G. Costantini, S. Rusponi, R. Gianotti, C. Boragno, U. Valbusa: Surf. Sci. **416**, 245 (1998)
40. C. Busse, H. Hansen, U. Linke, Th. Michely: Phys. Rev. Lett. **85**, 326 (2000)
41. R.M. Bradley, J.M.E. Harper: J. Vac. Sci. Technol. A **6**, 2390 (1988)
42. P. Sigmund, J. Mater. Sci. **8**, 1545 (1973)
43. R. Friedrich, G. Radons, T. Ditzinger, A. Henning: Phys. Rev. Lett. **85**, 4884 (2002)
44. S. Habenicht, W. Bolse, K.P. Lieb, K. Reimann, U. Geyer: Phys. Rev. B **60**, R2200 (1999)
45. I. Koponen, M. Hautala, O.P. Sievänen, Phys. Rev. Lett. **78**, 2612 (1997)
46. D.N. Bly, P.J. Rous: Phys. Rev. B **53**, 13909 (1996)
47. R.S. Sorbello: Solid State Phys. **51**, 159 (1998)
48. H. Dobbs, J. Krug: J. Phys. I France **6**, 413 (1996)

49. R.P. Johnson: Phys. Rev. A **54**, 459 (1938)
50. K. Yagi, H. Minoda, M. Degawa: Surf. Sci. Rep. **43**, 45 (2001)
51. G. Frohberg, P. Adam: Thin Solid Films **25**, 525 (1975)
52. S. Stoyanov: Jpn. J. Appl. Phys. **30**, 1 (1991)
53. O. Pierre-Louis: Surf. Sci. **529**, 114 (2003)
54. M. Degawa, H. Minoda, Y. Tanishiro, K. Yagi: Phys. Rev. B **63**, 045309 (2001)
55. M. Degawa, H. Minoda, Y. Tanishiro, K. Yagi: Surf. Sci. Lett. **461**, L528 (2000)
56. W.W. Mullins: J. Appl. Phys. **30**, 77 (1959)
57. P. Politi, J. Villain: Phys. Rev. B **54**, 5114 (1996)
58. J. Krug: Physica A **263**, 170 (1999)
59. J.E. Van Nostrand, S.J. Chey, D.G. Cahill: Phys. Rev. B **57**, 12536 (1998)
60. K.A. Bratland, Y.L. Foo, J.A.N.T. Soares, T. Spila, P. Desjardins, J.E. Greene: Phys. Rev. B **67**, 125322 (2003)
61. A.J. Bray: Adv. Phys. **43**, 357 (1994)
62. L. Golubović: Phys. Rev. Lett. **78**, 90 (1997)
63. M. Rost, J. Krug: Phys. Rev. E **55**, 3952 (1997)
64. M. Siegert: Physica A **239**, 420 (1997)
65. D. Moldovan, L. Golubovic: Phys. Rev. E **61**, 6190 (2000)
66. C. Castellano, J. Krug: Phys. Rev. B **62**, 2879 (2000)
67. P. Politi: Phys. Rev. E **58**, 281 (1998)
68. P. Politi, A. Torcini: J. Phys. A **33**, L77 (2000)
69. M.D. Johnson, C. Orme, A.W. Hunt, D. Graff, J. Sudijono, L.M. Sander, B.G. Orr: Phys. Rev. Lett. **72**, 116 (1994)
70. J. Krug, M. Plischke, M. Siegert: Phys. Rev. Lett. **70**, 3271 (1993)
71. M. Siegert, M. Plischke: Phys. Rev. Lett. **73**, 1517 (1994)
72. R.V. Kohn, X. Yan: Comm. Pure Appl. Math. **56**, 1549 (2003)
73. M. Siegert: Phys. Rev. Lett. **81**, 5481 (1998)
74. L.-H. Tang, P. Šmilauer, D.D. Vvedensky: Eur. Phys. J. B **2**, 409 (1998)
75. P. Šmilauer, M. Rost, J. Krug: Phys. Rev. E **59**, R6263 (1999)
76. J. A. Stroscio, D. T. Pierce, M.D. Stiles, A. Zangwill, L.M. Sander: Phys. Rev. Lett. **75**, 4246 (1995)
77. J. Krug: J. Stat. Phys. **87**, 505 (1997)
78. J. Krug, P. Kuhn: 'Second Layer Nucleation and the Shape of Wedding Cakes'. In: *Atomistic Aspects of Epitaxial Growth*, ed. by M. Kotrla, N.I. Papanicolaou, D.D. Vvedensky, L.T. Wille (Kluwer, Dordrecht 2002) pp. 145–163
79. J. Krug, P. Politi, T. Michely: Phys. Rev. B **61**, 14037 (2000)
80. T. Michely, M. Kalff, G. Comsa, M. Strobel, K.-H. Heinig: 'Coarsening Mechanisms in Surface Morphological Evolution'. In: *Atomistic Aspects of Epitaxial Growth*, ed. by M. Kotrla, N.I. Papanicolaou, D.D. Vvedensky, L.T. Wille (Kluwer, Dordrecht 2002) pp. 185–196
81. J.S. Langer, Ann. Phys. **65**, 53 (1971)
82. O. Pierre-Louis, C. Misbah, Y. Satio, J. Krug, P. Politi: Phys. Rev. Lett. **80**, 4221 (1998)
83. J. Kallunki, J. Krug: Phys. Rev. E **62**, 6229 (2000)
84. F. Gillet, O. Pierre-Louis, C. Misbah: Eur. Phys. J. B **18**, 519 (2000)
85. A. Pimpinelli, I. Elkinani, A. Karma, C. Misbah, J. Villain: J. Phys. Condens. Matter **6**, 2661 (1994)
86. P. Politi, C. Misbah: Phys. Rev. Lett. **92**, 090601 (2004)

87. S. Paulin, F. Gillet, O. Pierre-Louis, C. Misbah: Phys. Rev. Lett. **86**, 5538 (2001)
88. J. Krug: Adv. Compl. Sys. **4**, 353 (2001)
89. Y.-N. Yang, E.S. Fu, E.D. Williams: Surf. Sci. **356**, 101 (1996)
90. D.-J. Liu, J.D. Weeks: Phys. Rev. B **57**, 14891 (1998)
91. M. Sato, M. Uwaha: Surf. Sci. **442**, 318 (1999)
92. S. Stoyanov, V. Tonchev: Phys. Rev. B **58**, 1590 (1998)
93. K. Fujita, M. Ichikawa, S.S. Stoyanov: Phys. Rev. B **60**, 16006 (1999)
94. A. Pimpinelli, V. Tonchev, A. Videcoq, M. Vladimirova: Phys. Rev. Lett. **88**, 206103 (2002)
95. P. Nozières: J. Physique **48**, 1605 (1987)
96. D.-J. Liu, E.S. Fu, M.D. Johnson, J.D. Weeks, E.D. Williams: J. Vac. Sci. Technol. B **14**, 2799 (1996)
97. V. Tonchev, S. Stoyanov, J. Krug, A. Pimpinelli (in preparation)
98. J. Krug: 'Continuum Equations for Step Flow Growth'. In: *Dynamics of Fluctuating Interfaces and Related Phenomena*, ed. by D. Kim, H. Park, B. Kahng (World Scientific, Singapore 1997) pp. 95–113
99. R. Cuerno, A.-L. Barabási: Phys. Rev. Lett. **74**, 4746 (1995)
100. M. Rost, J. Krug: Phys. Rev. Lett. **75**, 3894 (1995)
101. G.I. Sivashinsky: Ann. Rev. Fluid Mech. **15**, 179 (1983)
102. Y. Kuramoto: *Chemical Osillations, Waves and Turbulence* (Springer, Berlin 1984)
103. P. Manneville: *Dissipative Structures and Weak Turbulence* (Academic Press, San Diego 1990)
104. T. Bohr, M.H. Jensen, G. Paladin, A. Vulpiani: *Dynamical Systems Approach to Turbulence* (Cambridge University Press, Cambridge, UK, 1998)
105. V. Yakhot: Phys. Rev. A **24**, 642 (1981)
106. K. Sneppen, J. Krug, M.H. Jensen, C. Jayaprakash, T. Bohr: Phys. Rev. A **46**, R7351 (1992)
107. B.M. Boghosian, C.C. Chow, T. Hwa: Phys. Rev. Lett. **83**, 5262 (1999)
108. S. Park, B. Kahng, H. Jeong, A.-L. Barabási: Phys. Rev. Lett. **83**, 3486 (1999)
109. A.A. Golovin, S.H. Davis, A.A. Nepomnyashchy: Phys. Rev. E **59**, 803 (1999)
110. A.A. Golovin, A.A. Nepomnyashchy, S.H. Davis, M.A. Zaks: Phys. Rev. Lett. **86**, 1550 (2001)
111. S.J. Watson, F. Otto, B.Y. Rubinstein, S.H. Davis: Physica D **178**, 127 (2003)
112. K. Leung: J. Stat. Phys. **61**, 345 (1990)
113. C.L. Emmott, A.J. Bray: Phys. Rev. E **54**, 4568 (1996)
114. Y. Saito, M. Uwaha: J. Phys. Soc. Jpn. **65**, 3576 (1996)